**NURETH14-028** 

# NUMERICAL SIMULATIONS OF UPPER PLENUM THERMAL-HYDRAULICS OF MONJU REACTOR VESSEL USING HIGH RESOLUTION MESH MODELS

## H. Ohira<sup>1</sup>, K. Honda<sup>1</sup> and M. Sotsu<sup>1</sup>

<sup>1</sup> Japan Atomic Energy Agency, Tsuruga, Fukui, Japan ohira.hiroaki@jaea.go.jp, honda.kei@jaea.go.jp, sotsu.masutake@jaea.go.jp

#### **Abstract**

In order to evaluate the upper plenum thermal-hydraulics of the Monju reactor vessel, we have performed detail calculations under the 40% rated power operational condition using high resolution mesh models by a commercial FVM code, FrontFlow/Red. In this study, we applied a high resolution meshes around the flow holes (FHs) on the inner barrel. We mainly made clear that the thermal-hydraulics did not change largely since the flow rates through the FHs were small enough to the total coolant flow rate but were affected largely in case without FHs on the honeycomb structure.

#### Introduction

The Japanese prototype fast breeder reactor Monju was started in May 2010 and the core confirmation tests were conducted for about three months as of July. The system start-up tests (SSTs) under 40% rated power and the power rising tests are also scheduled in near future. In these tests, the plant operation and control performance are mainly evaluated in order to verify the design concepts. The plant dynamics of simulated anticipated and abnormal transients such as a reactor manual scram, loss of off-site power, PHTS pump trip, natural circulation, etc. are also carried out and verified the design and safety assessment codes [1].

The thermal-hydraulics in the reactor vessel (RV) upper plenum such as thermal stratification in the post-scrum transients may cause severe thermal stress problems. Mock-up tests using water or sodium as the working fluid had been conducted to evaluate these phenomena and validated numerical simulation codes [2,3]. Detail calculations were not practicable because of the shortage of the computational power and numerical algorithm. Recently, the numerical analysis codes with highly advanced algorithms have been developed and the computational performances have been also progressed remarkably, by which thermal-hydraulic evaluations of large and complex regions have become practicable within reasonable computational costs. These codes are modelled by FVM and provided for highly accurate turbulence models and fast matrix solvers [4,5]. Hence, it is necessary to evaluate the thermal-hydraulics using these codes and apply to the future FBRs.

We already calculated the thermal-hydraulics under 40% rated power operational condition of Monju with a high resolution meshes and made sure the modelling and calculating techniques of huge computational models [4]. The temperature distributions on the thermocouple plug (TC-plug), which was installed in the vertical direction, agreed well with the SST results and the flow and temperature distributions also showed reasonable ones compared with the test results. In these calculation models, however, the flow holes (FHs) on the inner barrel had low grid resolutions and this might affect to the thermal stratification in the plenum, especially that in the post-scram

transient conditions. On the other hand, the FHs on the honeycomb structure (HS) installed between the core top and the upper instrument structure (UIS) were modelled as an average permeability: These FHs might also affect the thermal-hydraulics. Hence, it is necessary to evaluate these effects and select the proper model before the transient calculations. Along with our calculations, some calculations were carried out by member states under the Coordinate Research Project of IAEA (IAEA-CRP) [6,7]. Up to now, these calculations were performed using 1/6 sector models, however, three dimensional calculations with high resolution meshes are scheduled and these results are also presented in near future.

From these motivations described above, we modified the previous numerical model to an advanced one with high resolution meshes around the FHs on the inner barrel. We also modified it to another one without flow holes on the HS. These calculation results were compared with those presented in the previous paper and evaluated these effects. Using these results, we estimated the pressure loss coefficients of the FHs on the inner barrel and compared with the evaluated ones form the mock-up tests for Monju RV plenum.

## 1. Upper Plenum of Monju RV

The upper plenum of Monju RV is shown in Figure 1. UIS is installed in the center of the RV through the shield plug to the upper region of the core. Thermocouples are also installed through the UIS to the flow guide tubes (FGTs).

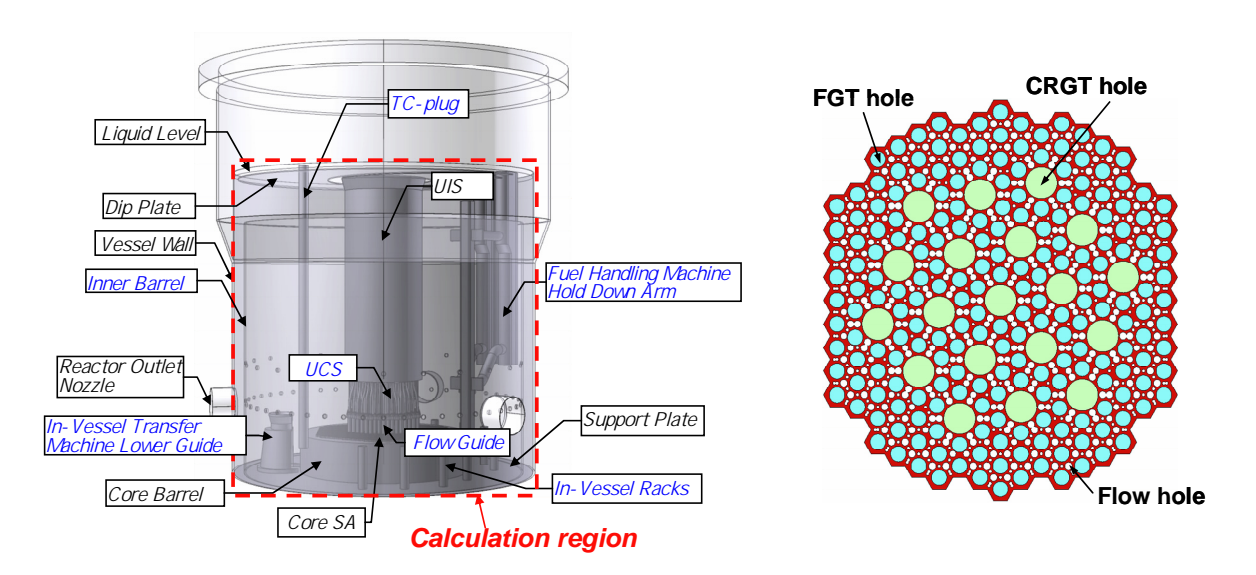


Figure 1 Monju RV upper plenum

Figure 2 Top view of Honeycomb structure

The HS supports these FGTs and control rod guide tubes (CRGTs), and is supported by the UIS. The HS has various kinds of FHs between these tubes, which are shown as white circles in Figure 2. The detail location of HS is illustrated in Figures 5(a) and 5(b). Hold Down Axis equipped with Hold Down Arms and TC-plug are also installed approximately 2,470 mm and 3,043 mm off-center of the RV, respectively, which support the fuel handling machine (FHM) and measure the temperature distribution in the vertical direction of the upper plenum. The inner barrel is set up on

the upper support plate in order to mitigate the severe thermal stress to the RV wall, which is mainly caused by the thermal stratification. However, flow holes 92 mm in diameter are opened in the circumferential direction in the different height of the inner barrel in order to decrease the rising speed of the thermal stratification front.

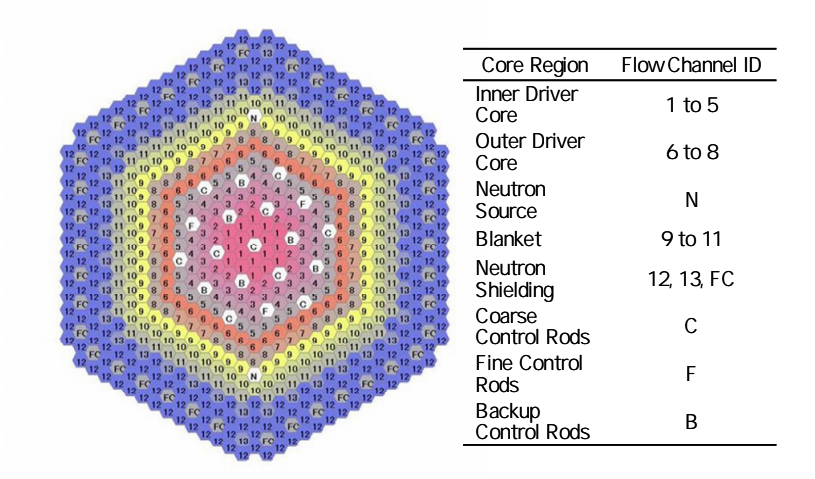


Figure 3 Top view of core subassemblies

On the other hand, Monju core has 108 and 90 fuel subassemblies as the inner and outer driver core, respectively, which also has 172 blanket and 324 neutron shielding subassemblies, etc. The top view of the Monju core is shown in Figure 3. In the upper plenum, 10 In-Vessel Racks and an In-Vessel Transfer Machine (IVTM) Lower Guide are set up on the upper support plate outside of this core. These details are reported in [8].

## 2. Calculation Models

#### 2.1 Governing equations

In this study, multi-dimensional thermal-hydraulic analysis code FrontFlow/Red [5], which was developed by University of Tokyo under the project of Revolutionary Simulation Software, was applied to the present calculations. The governing equations applied in this code were mass, momentum and energy conservation equations for incompressible fluid, which were discretized by FVM. The standard k- $\epsilon$  model with the re-normalization group theory (RNG k- $\epsilon$  model) [9] was also applied as the turbulence model, which was only added to the third term of the following turbulent dissipation equation;

$$\frac{\partial}{\partial t}(\rho\varepsilon) + \frac{\partial}{\partial x_{j}}(\rho\varepsilon u_{j}) = \frac{\partial}{\partial x_{j}} \left[ \left( \mu + \frac{\mu_{T}}{\sigma_{\varepsilon}} \right) \frac{\partial\varepsilon}{\partial x_{j}} \right] + \frac{\varepsilon}{k} \left( C_{\varepsilon 1} P_{k} - C_{\varepsilon 2} \rho\varepsilon \right) - \frac{C_{\mu} S^{3} (1 - S/S_{0})}{1 + \beta S^{3}} \frac{\varepsilon^{2}}{k} , \qquad (1)$$

where 
$$S = k\varepsilon^{-1} (S_{ij}S_{ji}/2)^{1/2}$$
,  $S_{ij} = \partial u_i/\partial x_j + \partial u_j/\partial x_i$ ,  $S_0 = 4.38$  and  $\beta = 0.012$ .

Buoyancy force was considered as the third terms in the momentum equation (2). Flow holes on the HS are too small compared to the plenum size to be modelled even by the present detailed grids. Hence, the HS was assumed as a porous medium; only these holes were modelled by porous media

approaches with pressure loss correlations, which were also added in the fourth terms of the equation (2);

$$\frac{\partial(\rho u_i)}{\partial t} + \frac{\partial(\rho u_i u_j)}{\partial x_j} = -\frac{\partial p}{\partial x_i} + \frac{\partial}{\partial x_j} \left[ \left( \mu + \mu_t \left( \frac{\partial u_i}{\partial x_j} + \frac{\partial u_j}{\partial x_i} \right) \right) \right] + \left( \rho - \rho_0 \right) g_i - \delta(z - z_0) K \frac{1}{2} \rho |u_i| u_i,$$
(2)

where  $z_0$  is the location of the bottom of the HS.  $\rho$ ,  $\mu$  and  $\rho$  are the density, viscosity and pressure of liquid sodium, respectively.  $\rho_0$  is the density at a reference temperature in the upper plenum.  $\mu_t$  is the turbulent viscosity ( $\mu_t = C_\mu k^2 / \varepsilon$ ) and K is the pressure loss coefficient which was evaluated and proposed as K = 25 [6].  $\delta(z)$  is the Dirac delta function.

## 2.2 Discretization of Governing Equations

FrontFlow/Red employs implicit methods to solve the algebraic finite volume equations for hexahedron, tetrahedron, triangular prism and square pyramid meshes using the general curvilinear coordinate system with the collocated grid arrangement of the variables, in which the velocity components and the pressure are defined at the cell center and the fluxes are defined on the cell-bounding surfaces. Rhie-Chow correction [10] is also used to remove oscillations in the pressure solutions. The fully-implicit scheme of SIMPLE method was applied to all equations in the present steady state calculations. The first order upwind and the second order central difference scheme were respectively applied to the advection and diffusion terms. ICCG for the pressure Poisson equation and BiCGSTAB for the other equations were also applied to the matrix solvers. In order to avoid converging to inadequate solutions and to accelerate convergence of the iterative process, a pseudo time-marching approach was applied in the present calculations: The discretized transient equations were solved by using under-relaxation factors.

## 3. Numerical conditions

#### 3.1 Calculation models

The region described by the dotted red line in Figure 1 was basically modelled in detail without any approximation, although only HS region was modelled with porous media approaches as described in the section 3: The shapes of the outlets of core subassembly, FHM, TC-plug, In-Vessel Racks and IVTM Lower Guide were modelled in detail by using hexahedron, tetrahedron, triangular prism and square pyramid meshes. These models and the close-up views of the FHs are shown in Figure 4.

The close-up views in the UCS region and around HS are also shown in Figures 5(a) and 5(b), respectively. The red painted region is the HS and flow holes opened between the FGTs and CRGTs were modelled by the porous media approaches and calculated by Equation 2. These models were constructed by using the data described in [8]. The total number of the mesh increased to approximately 18 millions of which the maximum and minimum sizes were 50.0 mm near the sodium surface and 3.0 mm in the UCS region, respectively.

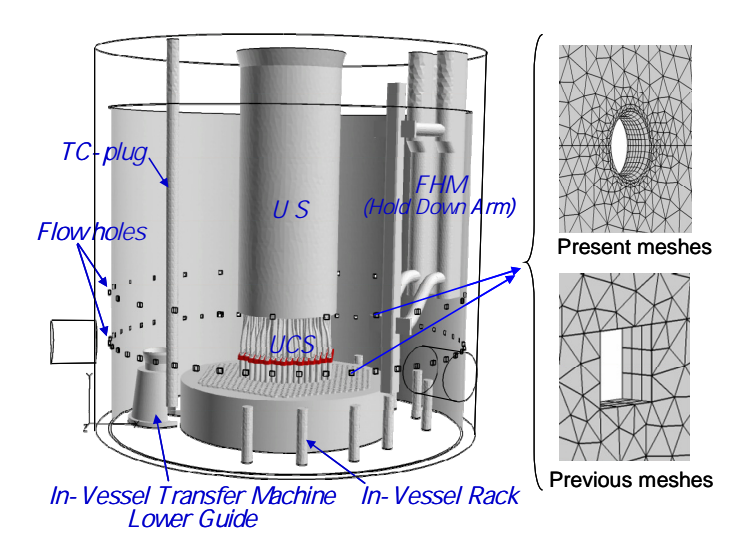
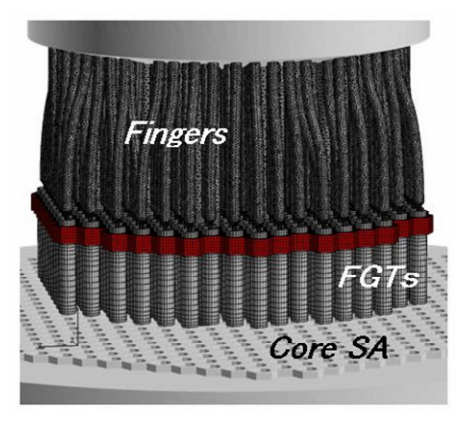


Figure 4 Analytical model of Monju RV upper plenum



Fingers

HS

FGTs

Fig. 5(a) Close-up view of UCS region

Fig. 5(b) Close-up view around HS

#### 3.2 Boundary and initial conditions

We applied the detail mesh around the flow holes in the present study. The velocity condition on the structure surfaces was given as logarithmic law (log-law) conditions in all the cases. The thermal conduction calculation with heat transfer correlations was performed for the inner barrel. In the previous calculations, every flow hole on the inner barrel was composed of 27 hexahedron meshes, however, it had approximately 2300 tetrahedrons in the present calculations. The flow rates of the outlets of core subassembly were also given as the 40% rated operational conditions that were also described in [8], while those of the RV outlet nozzles were free outlet conditions.

The temperature conditions on the structure surfaces except for the inner barrel and the upper support plate were assumed as adiabatic conditions. On the other hand, the inner barrel surfaces were assumed as a heat transfer conditions. The heat transfer correlations of Equation 3 were given on the surfaces of the inner barrel for the thermal conduction calculations in all the cases.

$$Nu = \begin{cases} 3.64 & (Pe < 47.5) \\ 5.0 + 0.038 \cdot Pe^{0.68} & (Pe \ge 47.5) \end{cases}$$
 (3)

where Nu and Pe is Nusselt and Peclet number whose characteristic lengths were given as the distance between the neighbouring cell center and the surface of the inner barrel which was measured in the previous SSTs. The flow holes on the HS were applied the same porous model of the previous calculations in Case 1, while those were neglected in Case 2. The temperature on support plate was assumed 375°C. The initial temperatures were 477°C and initial velocities were zeros in the upper plenum. When we started with buoyancy term in the momentum equations from reposing fluid with constant temperature of 513, 380 and 477°C, the jet from the lower part of UIS did not reach to the inner barrel but reached to the sodium surface. The solutions could not change to the momentum driven solutions at least more 30 to 50 thousand time steps. However, we have already estimated from many scaled tests using sodium and water that the momentum driven solutions were close to the actual behaviour [2,12]. The temperature distribution on TC-plug in the Monju-RV also indicate the solution; the buoyancy driven solution cannot be explained the temperature change in the middle part of the plug (ca -4000 to ca -3000 mm from sodium surface as shown in Figure 9). Both temperature and velocity in the upper plenum, especially near the core outlet, increase rapidly and the abnormal phenomena appear in such initial conditions: Large buoyancy force is calculated in the initial phase. In order to resolve above problem, we calculated momentum equations without buoyancy term for After that, we restarted with the buoyancy force. about 10 thousand steps. calculations, the pseudo time step and Courant number were 0.1 and approximately 110, respectively.

#### 4. Results and discussions

## 4.1 Temperature and Velocity Distribution in the upper plenum

Temperature distribution on the vertical cross section VCS-1, VCS-2 and VCS-3 are shown in Figures 6(a), 6(b) and 6(c), respectively. The locations of the cross sections are shown in the upper part of these figures and VCS-1 is the same one as presented in [4]. These temperature distributions in the upper region were similar to each other, however, those in the lower part of FHM on VCS-3 became lower than the others.

Temperature distributions on the horizontal cross section (HCS) at the different steps in the steady state are shown in Figures 7(a), 7(b) and 7(c), whose height is also shown in the upper part of Figure 6. The velocity and temperature distributions changed in every step even after the steady state had been reached. Hence, these figures were described in every 2,000 step interval including the last calculation step, which were Steps 1, 2 and 3, respectively. Temperature below the FHM became lower in every step, while that in the other region changed in the different steps. Sodium flows out obliquely upward direction to the upper area of the upper FHs of the inner barrel. From this region, the flow is divided into the upward and downward direction along the inner barrel in the region without FHM. The downward flow, which partially flows out from the two levels of the flow holes, mainly re-circulates to the core top region and mixes with colder sodium above the upper plate. In the region around FHM, however, the colder sodium cannot be mixed enough with the hotter one, since most of the jet flows in the upward direction.

The velocity distributions on VCS-2 and VCS-3 at Step 1 are shown in Figures 8(a) and 8(b), respectively. The symmetrical distributions were calculated on VCS-2 at Step 1, while the slope of the jet in the left region became larger than that in the right region on VCS-3. However, the asymmetry disappeared at Step 2 as shown in Figure 8(c). These profiles also indicate the fluctuating velocity fields in the steady state conditions.

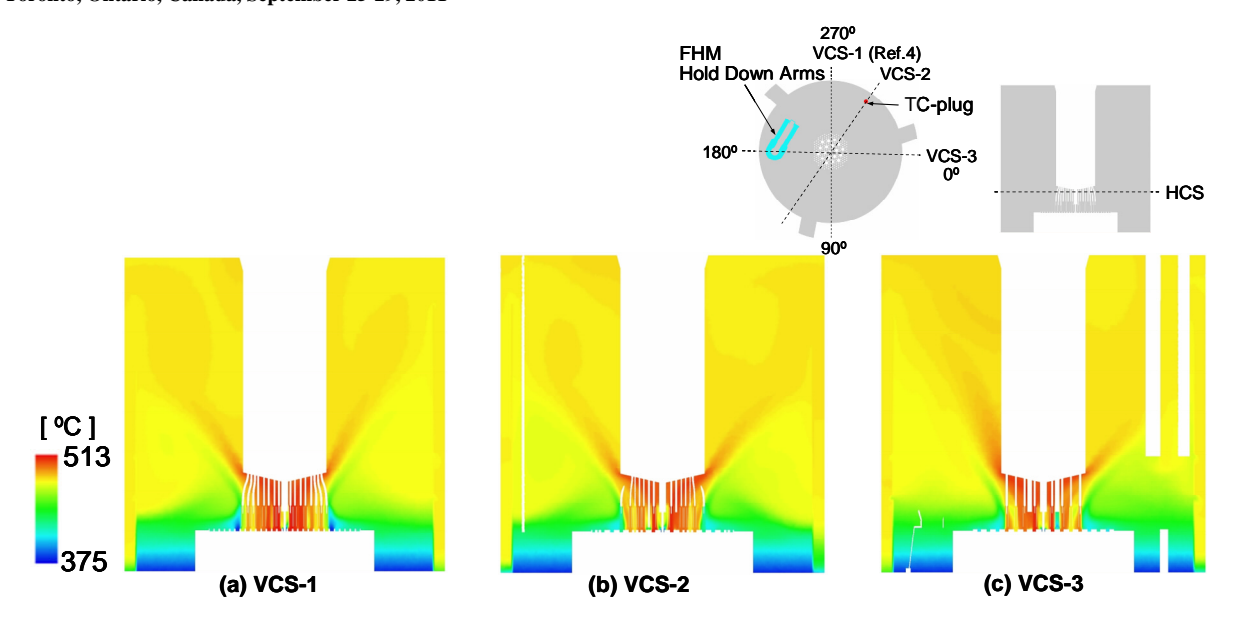


Figure 6 Temperature distributions on VCSs

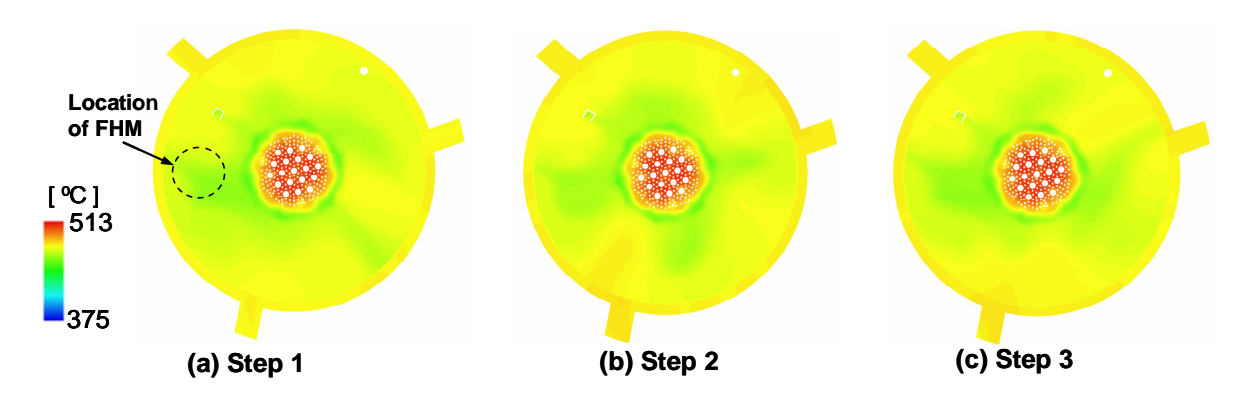


Figure 7 Temperature distributions on HCS at different steps

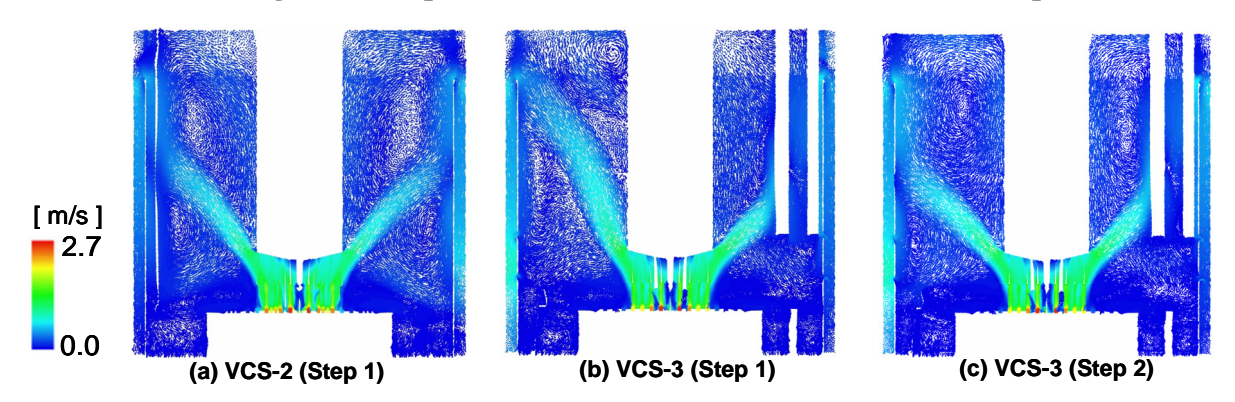


Figure 8 Velocity distributions on VCSs at different steps

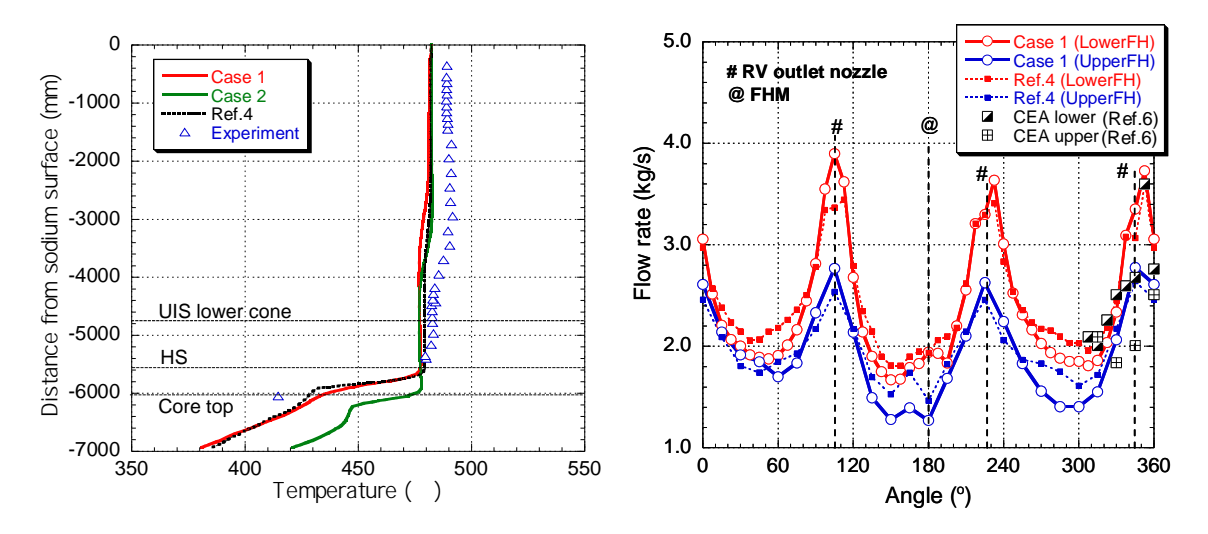


Figure 9 Temperature on TC-plug

Figure 10 Flow rate of FHs on inner barrel

## 4.2 Effects of high resolution mesh around flow holes

In the present study, we applied relatively high resolution meshes around the FHs on the inner barrel in Case 1, while low resolution ones in the previous calculation. Each flow rate of the FH was evaluated by integrating the flow rate calculated on the node. Both results are shown in Figure 10. The abscissa shows the angle of the FH centers in the RV circumferential direction. The typical angles are also shown in the upper part of Figure 6. The locations of the FHM and the RV outlet nozzles are also described in this figure.

In Case 1 calculation, the flow rates of the upper FHs were in the range from 1.2 to 2.8 kg/s, while those of the lower ones were in the range from 1.8 to 3.9 kg/s. These flow rates near RV outlet nozzles became larger than the others. It is considered that these distributions were caused by the negligible circumferential pressure drops between the inner barrel and RV wall. On the other hand, the flow rates of near-FHM flow holes became smaller than the others, since the downward flow along the inner barrel in the region near FHM became smaller than that in the other region. The flow rate in the previous calculation with rough meshes around FHs showed quite similar tendency and amounts to those in Case 1, although the maximum and minimum values had some differences.

Table 1 Total flow rate and flow ratio of FHs

14010 1 10001 110 () 1400 4110 11 14010 01 1 110				
	Upper FHs		Lower FHs	
	Flow rate (kg/s)	Percentage (%)	Flow rate (kg/s)	Percentage (%)
Case 1	46.0	2.3	113.8	5.6
Previous	47.3	2.3	117.2	5.8

The total flow rates of the upper and lower FHs in both calculations are summarized in Table 1. The percentages of the flow rates in the upper and lower FHs to the total inflow rate from the core were approximately 2.3% and 5.6%, respectively in Case 1 and approximately 2.3% and 5.8%, respectively in the previous calculation. These percentages were almost equal in both results in spite of different

resolutions around the FHs, because the velocity boundary conditions on the inner surfaces of the FHs were given as the log-low whose friction velocities were defined on the surfaces. The calculated volume flow rates described in [6] are evaluated using sodium density at 480°C also plotted in Figure 10. The 1/6 sector model with high resolution meshes around FHs was applied in these calculations. Our present results and previous ones agreed well with the 1/6 sector model results. In the present steady state conditions, all the percentages are so small that these differences might not largely affect to the thermal-hydraulics in the upper plenum. However, the percentages might become larger and the effects could not be negligible in the lower flow rate conditions such as scrum transients and natural circulations.

Figure 11 shows the pressure loss coefficients calculated by Equation 4 using above-mentioned flow rates and the pressure differences between the outside and inside of flow holes. The coefficients of the previous rough meshes are also plotted in this figure.

$$\langle \Delta P \rangle = \xi \frac{1}{2} \rho \langle u \rangle^2 \,, \tag{4}$$

where  $\langle u \rangle$  is the average flow rate through a FH,  $\langle \Delta P \rangle$  is the pressure difference between the inside and the outside of a flow hole with identical areas to the flow holes, and  $\xi$  is the pressure loss coefficient.

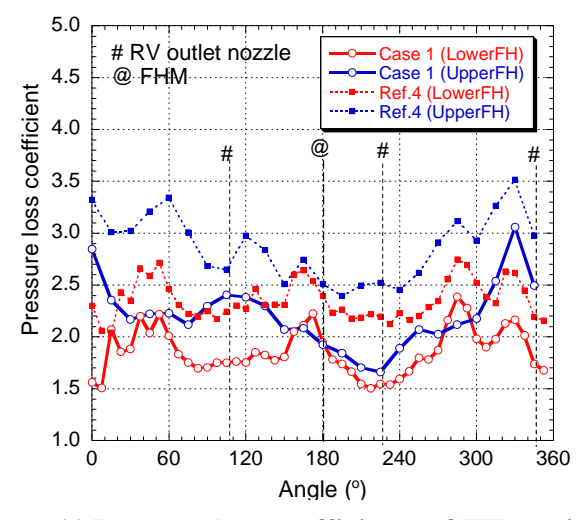


Figure 11 Pressure loss coefficients of FHs on inner barrel

The average coefficients of the upper flow holes and the lower ones in Case 1 were approximately 2.2 and 1.9, respectively, while those in the previous calculations were approximately 2.9 and 2.4, respectively: The average coefficients of Case 1 were approximately 30% larger than those of the previous study, while flow rates of the two showed similar values. These results indicate that the coefficient becomes very sensitive because both pressure drop and velocity fluctuate at every step in the calculations. The coefficient of 1.6 was evaluated in the mock-up tests, which was mainly for the scram transients conditions of the lower FHs [2,12]. The present Case 1 model resulted close coefficient, however, it is estimated higher order scheme in the temporal and advection terms should be applied to all equations for the accurate predictions. These coefficients should be also evaluated by other results under different conditions such as the rated operational conditions and scram transient ones.

### 4.3 Thermal-hydraulics without flow holes on the honeycomb structure

Figure 12(b) shows the velocity distribution of Case 1 on the vertical lines described in Figure 12(a), which shows outflow distributions in the radial direction from the UCS region. Sodium mainly flows out from the upper region of the HS, especially from the bottom of UIS: it does not flow out from the lower region. These distributions are similar to each other in the circumferential direction, which indicates that the outflow distributions in the circumferential direction are similar even if the jets have different slopes as shown in Figure 9; the slopes are caused not by the outflow distribution but by the velocity changes in the upper plenum.

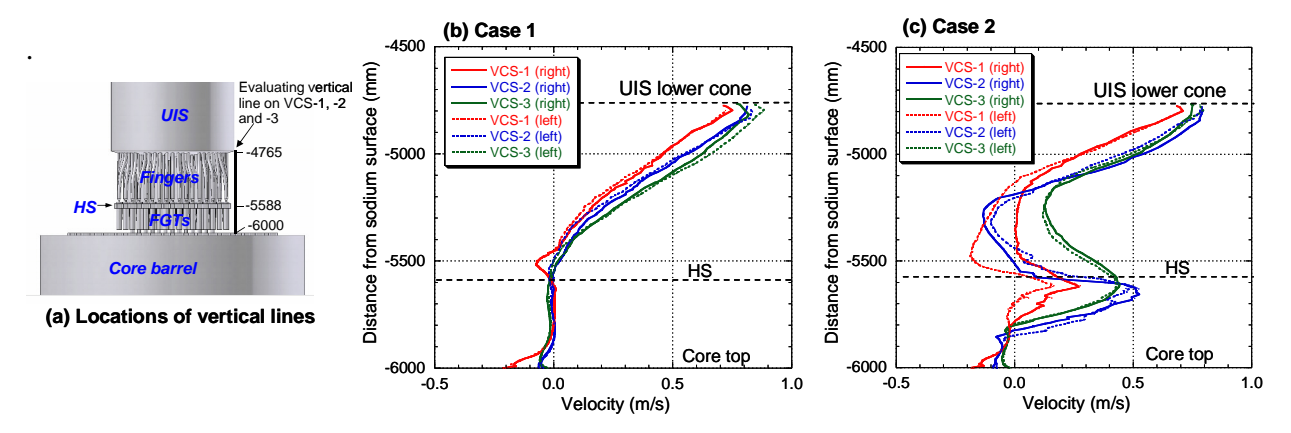


Fig. 12 Velocity distributions on vertical line along HS

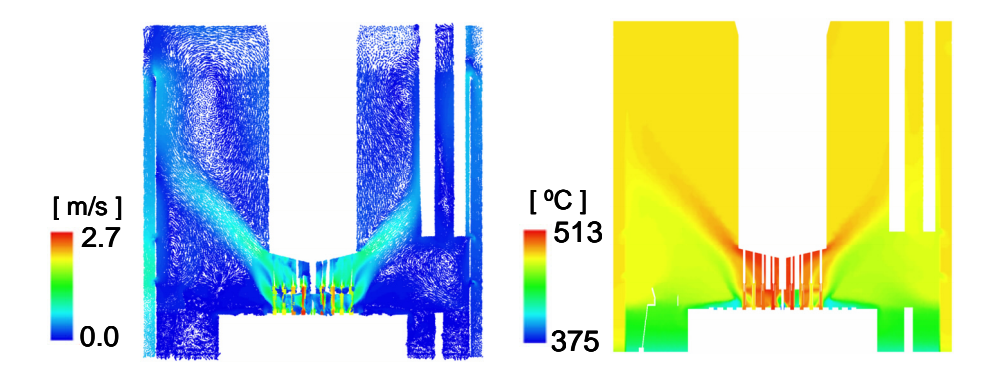


Figure 13 Velocity and temperature distributions on VCS-3 without FHs on HS

In case without flow holes on the HS (Case 2), however, the velocity in the radial direction appears below the HS and the amounts from the upper region become smaller, which are shown in Figure 12(c). This might be caused by the transverse velocity below the HS which cannot flow into the FGTs but flow out to the upper plenum

The velocity and temperature distributions on VCS-3 are shown in Figures 13(a) and 13(b), respectively. The slope of the jet in Case 2 becomes smaller than that in Case 1 and the temperature around the core barrel become higher. Colder sodium flowed out from the neutron shielding and blanket subassemblies mixed directly with hotter sodium, and flowed out from the lower region of HS. Eventually, the mixture was transported to the core side region. These temperatures on TC-plug also became higher than measured temperatures as shown in Figure 9.

From the results shown above, it becomes clear that the proper estimations of the pressure loss coefficients on the HS are also important because the coefficients affect to the thermal-hydraulics in the upper plenum.

#### 5. Conclusions

In order to evaluate the thermal-hydraulic behavior in the RV upper plenum of Monju, we have performed detail calculations in the 40% rated power operational condition using high resolution mesh models. In this study, we modified these models with high resolution meshes around FHs on the inner barrel and calculated the behavior. We also assumed the HS had no FHs and evaluated the effects. The following results were made clear through these calculations;

- (1) In the 40% rated power operational condition, the thermal-hydraulics of the upper plenum did not change largely in spite of using high resolution meshes around FHs on the inner barrel since the flow rates through the FHs were small enough to the total coolant flow rate,
- (2) The average pressure loss coefficient of the lower FHs was approximately 1.9, which was close to the previous R&D experiments of 1.6. This result indicated the importance of higher order scheme in the temporal and advection terms of the governing equations, and
- (3) In the case without FHs on the HS, hotter sodium flows out below the HS and coolant temperatures beside the core barrel became higher than those measured in the SSTs and those calculated in Case 1 and the thermal-hydraulics were affected largely.

Using present high resolution mesh model, we are going to perform scrum transient calculations from this 40% rated power condition and to evaluate the thermal stratification behavior in the upper plenum.

## 6. Acknowledgments

The authors would like to acknowledge Dr. H. Zhang, President of Numerical Flow Designing Co., Ltd., for his help of the present calculations and the mesh constructing. The authors would also like to acknowledge the following Chief Scientific Investigators (CSIs) of IAEA's Monju-CRP for their discussions and the authors reporting calculation results for the meeting,

- Mr. Y. Xu, China National Nuclear Corp. (CNNC), China Institute of Atomic Energy (CIAE); Department of China Experimental Fast Reactor.
- Mr. F. Ducros, Commissariat àl'énergie atomique (CEA), Centre de Saclay.
- Mr. K. Velusamy, Indira Gandhi Centre for Atomic Research (IGCAR).
- Mr. S. Yoshikawa, Japan Atomic Energy Agency (JAEA).
- Mr. S. K. Choi, Korea Atomic Energy Research Institute (KAERI).
- Mr. R. Wigeland, Idaho National Laboratory (INL).
- Mr. T. Sofu, Argonne National Laboratory (ANL).
- Mr. A. Stanculescu, CRP Scientific Secretary (IAEA).

#### 7. References

- [1] M. Konomura, M. Ichimiya and K. Mukai, "Future R&D programs using MONJU," International Conference on Fast Reactors and Related Fuel Cycles (FR09), No. IAEA-CN-176-01-11, December (2009).
- [2] Y. Ieda, I. Maekawa, T. Muramatsu and S. Nakanishi, "Experimental and Analytical Studies of the Thermal Stratification Phenomenon in the Outlet Plenum of Fast Breeder Reactors," Nuclear Engineering and Design, 120, pp. 403-414 (1990).
- [3] I. Maekawa, "Numerical Diffusion in Single-Phase Multi-Dimensional Thermal-Hydraulic Analysis," Nuclear Engineering and Design, 120 pp.323-339 (1990).
- [4] K. Honda, H. Ohira, M. Sotsu and S. Yoshikawa, "Thermal-hydraulic Analysis of MONJU Upper Plenum under 40% Rated Power Operational Condition," Proceedings of the 8th International Topical Meeting on Nuclear Thermal-Hydraulics, Operation and Safety (NUTHOS-8), Shanghai, China, October 10-14 (2010).
- [5] M. Tsubokura, T. Kobayashi, T. Nakashima, T. Nouzawa, T. Nakamura, H. Zhang, K. Onishi, N. Oshima, "Computational visualization of unsteady flow around vehicles using high performance computing," Computers & Fluids, 38 (2009) pp. 981–990.
- [6] V. Blind, U. Bieder and T. Sofu, "Benchmark Analysis of Sodium Natural Convection in the Upper Plenum of the MONJU Reactor Vessel: Preparation of a simplified model for the Upper Core Structures," DEN/CAD/DER/SSTH/LMDL/NT/2009-105/A, under Supervisory of Technical Working Group on Fast Reactors, International Atomic Energy Agency.
- [7] T. Sofu, J. Thomas and T. Fanning, "Analysis of Thermal Stratification in the Upper Plenum of the MONJU Reactor Vessel using a Simplified Model," Second Research Coordination Meeting IAEA Coordinated Research Project on "Benchmark Analysis of MONJU Natural Convection", 12-14 October 2009, Marcoule, FRANCE.
- [8] S. Yoshikawa and M. Minami, "Data Description for Coordinated Research Project on Benchmark Analyses of Sodium Natural Convection in the Upper Plenum of the MONJU Reactor Vessel under Supervisory of Technical Working Group on Fast Reactors, International Atomic Energy Agency," JAEA-Data/Code 2008-024, Japan Atomic Energy Agency (2009).
- [9] V. Yakhot, S. A. Orszag, S. Thangam, T. B. Gatski and C.G. Speziale, "Development of turbulence models for shear flows by a double expansion technique," Phys. Fluids, A4(7), pp. 1510-1520 (1992).
- [10] C.M. Rhie and R.L. Chow, "Numerical study of the turbulent flow past an airfoil with trailing edge separation," AIAA J., 21, pp.1525-1532 (1983).
- [11] Y. Doi, T. Muramatsu and K. Kunoki, "Thermal Stratification Tests in Monju Upper Plenum (I) –Temperature Distributions under Normal and Scram Conditions with 40% Power Operation-," PNC TN9410 96-117, May 1996 (In Japanese).
- [12] Y. Ieda, I. Maekawa, H. Ninokata and S. Nakanishi, "Investigation of Thermal Stratification Phenomena in Reactor Vessels (1) –Evaluation Methods on Thermal Stratification Phenomena-," PNC TN9410 86-007 (1986) (in Japanese).